International Journal of Mechanical, Industrial and Aerospace Sciences
ISSN: 2517-9950
Vol:14, No:5, 2020

Finite Element Analysis of Thermally-Induced Bistable Plate Using Four Plate Elements

Jixiao Tao, Xiaoqiao He

***Abstract*—**The present study deals with the finite element (FE) analysis of thermally-induced bistable plate using various plate elements. The quadrilateral plate elements include the 4-node conforming plate element based on the classical laminate plate theory (CLPT), the 4-node and 9-node Mindlin plate element based on the first-order shear deformation laminated plate theory (FSDT), and a displacement-based 4-node quadrilateral element (RDKQ-NL20). Using the von-Karman's large deflection theory and the total Lagrangian (TL) approach, the nonlinear FE governing equations for plate under thermal load are derived. Convergence analysis for four elements is first conducted. These elements are then used to predict the stable shapes of thermally-induced bistable plate. Numerical test shows that the plate element based on FSDT, namely the 4-node and 9-node Mindlin, and the RDKQ-NL20 plate element can predict two stable cylindrical shapes while the 4-node conforming plate predicts a saddles shape. Comparing the simulation results with ABAQUS, the RDKQ-NL20 element shows the best accuracy among all the elements.

***Keywords*—**Finite element method, geometrical nonlinearity, bistable, quadrilateral plate elements.

I. Introduction

BISTABLE or multi-stable plates and shells have many potential applications in morphing structures and broadband energy harvesting, and have attracted much research attention over the last few decades. Commonly, bistable plates have two stable configurations and can transform from one equilibrium position to another in response to a small energy input. Because no external forces are needed to sustain the equilibrium configuration, they are good candidates for morphing skins in aerospace applications [1], wind-harvesting technology [2], and automobile construction [3]. In addition, bistable plates can be bonded with piezoelectric layers to create an energy harvester that can realize broadband energy harvesting [4], [5]. Internal structural bistability will make it possible to design small and portable piezoelectric energy harvesters in the future.

Thermally-induced bistability is generally achieved by curing flat asymmetric laminates from high temperatures to room temperature. During the cooling process, thermal residual stresses accumulate due to the mismatch of thermal expansion coefficients among cross-ply layers, which eventually lead to two stable shapes. Hyer [6] first explored these bistable behaviors in the early 1980s. At that time, laminates with an unsymmetric stacking sequence were avoided in manufacturing, due to the bending-stretching coupling effect. To qualify this effect, Hyer et al. [7] developed an analytical model based on Kirchoff hypothesis with von Kármán geometric nonlinear strain in the CLPT. Two stable shapes were predicted using Rayleigh-Ritz minimization of the total potential energy in conjunction with polynomial approximations of the mid-plane strains. Since then, increasing numbers of researchers have studied bistable structures. The literatures in this area now include predicting stable shapes [8]-[10], calculating snap-through forces [11]-[13] and proposing new types of bistable structures [14]-[17].

In order to study the bistablility and energy harvesting performances of bistable plate, an accurate mathematical model is necessary. Previous theoretical studies on bistable plate are mainly based on analytical model. In this model, Rayleigh-Ritz method is used to approximate displacement filed, and Hamilton's principle is adopted to derive the equation of motion [12], [18]. Although the analytical model can achieve fast simulation, its' accuracy in dynamic analysis is still questionable. Diaconu et al. [12] used a second-order polynomial to approximate the out-of-plane displacement of bistable plate and found that it over-predicts the snap-through load by 30% compared to FE analysis and experiments. Betts et al. [18] used Diaconu's model to predict the harvested energy of bistable plate and found that it consistently over-predicts the power output by ~15%. In order to settle the limitations mentioned above, an accurate nonlinear FE model that can achieve fast simulation is necessary.

II. Classical and First-Order Theories of Laminated Composite Plates

A. CLPT

In the CLPT, Kirchhoff hypothesis is assumed that the transverse displacement is independent of the thickness coordinate, the transverse normal strain and the transverse shear stains are zero. The nonlinear strain-displacement relations are given by

$$\begin{Bmatrix}\varepsilon_{xx}\\ \varepsilon_{yy}\\ \gamma_{xy}\end{Bmatrix}=\boldsymbol{\varepsilon}_{\mathbf{m}}^{\mathbf{0}}+\boldsymbol{\varepsilon}_{\mathbf{b}}^{\mathbf{0}}+z\mathbf{k}=\begin{Bmatrix}\frac{\partial u_0}{\partial x}\\ \frac{\partial v_0}{\partial y}\\ \frac{\partial u_0}{\partial y}+\frac{\partial v_0}{\partial x}\end{Bmatrix}+\begin{Bmatrix}\frac{1}{2}\left(\frac{\partial w_0}{\partial x}\right)^2\\ \frac{1}{2}\left(\frac{\partial w_0}{\partial y}\right)^2\\ \frac{\partial w_0}{\partial x}\frac{\partial w_0}{\partial y}\end{Bmatrix}+z\begin{Bmatrix}-\frac{\partial^2 w_0}{\partial x^2}\\ -\frac{\partial^2 w_0}{\partial y^2}\\ -2\frac{\partial^2 w_0}{\partial x\partial y}\end{Bmatrix} \quad (1)$$

Jixiao Tao is with the City University of Hongkong, Tat Chee Avenue, Kowloon, Hong Kong, China (corresponding author, phone: 852-56430565; e-mail: jixiaotao2-c@ my.cityu.edu.hk).

Xiaoqiao He is with the City University of Hongkong, Tat Chee Avenue, Kowloon, Hong Kong, China (e-mail: bcxqhe@cityu.edu.hk).

where u_0 , v_0 and w_0 are the corresponding mid-plane displacement components.

Consider a composite laminate of total thickness *h* composed of *N* orthotropic layers with the principal material coordinates $\left(x_1^k, x_2^k, x_3^k\right)$ of the *k*th lamina oriented at an angle θ to the laminate coordinate, (x, y, z) , as shown in Fig. 1. When thermal effect is included, the linear constitutive relations for the *k*th orthotropic lamina in the laminate coordinates are

$$\begin{Bmatrix}\sigma_{xx}\\ \sigma_{yy}\\ \sigma_{xy}\end{Bmatrix}^{(k)}=\begin{bmatrix}\overline{Q}_{11} & \overline{Q}_{12} & \overline{Q}_{16}\\ \overline{Q}_{12} & \overline{Q}_{22} & \overline{Q}_{26}\\ \overline{Q}_{16} & \overline{Q}_{26} & \overline{Q}_{66}\end{bmatrix}^{(k)}\left(\begin{Bmatrix}\varepsilon_{xx}\\ \varepsilon_{yy}\\ \varepsilon_{xy}\end{Bmatrix}-\begin{Bmatrix}\alpha_{xx}\\ \alpha_{yy}\\ 2\alpha_{xy}\end{Bmatrix}\Delta T\right) \tag{2}$$

where $\overline{Q}_{ij}^{(k)}$ are the reduced transformed stiffness terms of the *k*th layer that can be expressed as

$$\begin{aligned}
\overline{Q}_{11} &= Q_{11}\cos^4\theta + 2\left(Q_{12}+2Q_{66}\right)\sin^2\theta\cos^2\theta + Q_{22}\sin^4\theta\\
\overline{Q}_{12} &= \left(Q_{11}+Q_{22}-4Q_{66}\right)\sin^2\theta\cos^2\theta + Q_{12}\left(\sin^4\theta+\cos^4\theta\right)\\
\overline{Q}_{22} &= Q_{11}\sin^4\theta + 2\left(Q_{12}+2Q_{66}\right)\sin^2\theta\cos^2\theta + Q_{22}\cos^4\theta\\
\overline{Q}_{16} &= \left(Q_{11}-Q_{12}-2Q_{66}\right)\sin\theta\cos^3\theta + \left(Q_{12}-Q_{22}+2Q_{66}\right)\sin^3\theta\cos\theta\\
\overline{Q}_{26} &= \left(Q_{11}-Q_{12}-2Q_{66}\right)\sin^3\theta\cos\theta + \left(Q_{12}-Q_{22}+2Q_{66}\right)\sin\theta\cos^3\theta\\
\overline{Q}_{66} &= \left(Q_{11}+Q_{12}-2Q_{12}-2Q_{66}\right)\sin^2\theta\cos^2\theta + Q_{66}\left(\sin^4\theta+\cos^4\theta\right)
\end{aligned} \tag{3}$$

and α_{xx} , α_{yy} , and α_{xy} are the transformed thermal coefficients of expansion

$$\begin{aligned}
\alpha_{xx} &= \alpha_1\cos^2\theta + \alpha_2\sin^2\theta\\
\alpha_{yy} &= \alpha_1\sin^2\theta + \alpha_2\cos^2\theta\\
2\alpha_{xy} &= 2\left(\alpha_1-\alpha_2\right)\sin\theta\cos\theta
\end{aligned} \tag{4}$$

Combining (1) and (2), and integrating over the laminate thickness, it is possible to obtain the equations of force and moment resultants as

$$\mathbf{N} = \mathbf{A}\boldsymbol{\varepsilon}^0 + \mathbf{B}\boldsymbol{\kappa} - \mathbf{N}^{\mathbf{T}} \tag{5}$$

$$\mathbf{M} = \mathbf{B}\boldsymbol{\varepsilon}^0 + \mathbf{D}\boldsymbol{\kappa} - \mathbf{M}^{\mathbf{T}} \tag{6}$$

where $\boldsymbol{\varepsilon}^0 = \boldsymbol{\varepsilon}_{\mathbf{m}}^0 + \boldsymbol{\varepsilon}_{\mathbf{b}}^0$; $\mathbf{A}$, $\mathbf{B}$ and $\mathbf{D}$ are laminate extensional, coupling and bending stiffness matrices, which are obtained by

$$\left(\mathbf{A},\mathbf{B},\mathbf{D}\right) = \sum_{k=1}^{N}\overline{Q}_{ij}^{(k)}\left(\left(z_{k+1}-z_k\right),\frac{1}{2}\left(z_{k+1}^2-z_k^2\right),\frac{1}{3}\left(z_{k+1}^3-z_k^3\right)\right) \tag{7}$$

and $\mathbf{N}^{\mathbf{T}}$, $\mathbf{M}^{\mathbf{T}}$ are the thermal force resultants

$$\left(\mathbf{N}^{\mathbf{T}},\mathbf{M}^{\mathbf{T}}\right) = \sum_{k=1}^{N}\int_{z_k}^{z_{k+1}}\left[\overline{Q}\right]^{(k)}\{\alpha\}^{(k)}\Delta T(1,z)\,dz \tag{8}$$

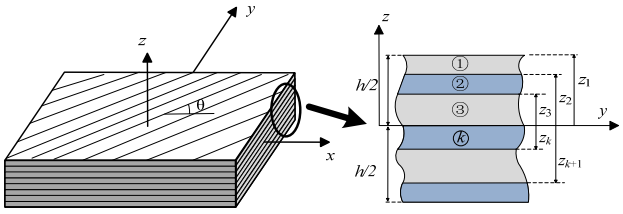

Fig. 1 Coordinate system and layer numbering used for a laminated plate

B. FSDT

In the FSDT, the strains have the form

$$\begin{Bmatrix}\varepsilon_{xx}\\ \varepsilon_{yy}\\ \gamma_{xy}\end{Bmatrix} = \boldsymbol{\varepsilon}_{\mathbf{m}}^0 + \boldsymbol{\varepsilon}_{\mathbf{b}}^0 + z\mathbf{k} = \begin{Bmatrix}\dfrac{\partial u_0}{\partial x}\\ \dfrac{\partial v_0}{\partial y}\\ \dfrac{\partial u_0}{\partial y}+\dfrac{\partial v_0}{\partial x}\end{Bmatrix} + \begin{Bmatrix}\dfrac{1}{2}\left(\dfrac{\partial w_0}{\partial x}\right)^2\\ \dfrac{1}{2}\left(\dfrac{\partial w_0}{\partial y}\right)^2\\ \dfrac{\partial w_0}{\partial x}\dfrac{\partial w_0}{\partial y}\end{Bmatrix} + z\begin{Bmatrix}\dfrac{\partial \theta_y}{\partial x}\\ \dfrac{\partial \theta_x}{\partial y}\\ \dfrac{\partial \theta_y}{\partial y}+\dfrac{\partial \theta_x}{\partial x}\end{Bmatrix} \tag{9}$$

$$\begin{Bmatrix}\gamma_{xz}\\ \gamma_{yz}\end{Bmatrix} = \boldsymbol{\gamma} = \begin{Bmatrix}\dfrac{\partial w_0}{\partial y}\\ \dfrac{\partial w_0}{\partial x}\end{Bmatrix} + \begin{Bmatrix}\theta_x\\ \theta_y\end{Bmatrix} \tag{10}$$

where θ_x and θ_y are the rotations of a transverse normal about the *y*- and *x*-axes, respectively.

The stress resultants are related to the generalized displacements by the relations

$$\begin{Bmatrix}\mathbf{N}\\ \mathbf{M}\\ \mathbf{T}\end{Bmatrix} = \begin{bmatrix}\mathbf{A} & \mathbf{B} & \mathbf{0}\\ \mathbf{B} & \mathbf{D} & \mathbf{0}\\ \mathbf{0} & \mathbf{0} & \mathbf{A_s}\end{bmatrix}\begin{Bmatrix}\boldsymbol{\varepsilon}^0\\ \mathbf{k}\\ \boldsymbol{\gamma}\end{Bmatrix} - \begin{Bmatrix}\mathbf{N}^T\\ \mathbf{M}^T\\ \mathbf{0}\end{Bmatrix} \tag{11}$$

The matrices $\mathbf{A}$, $\mathbf{B}$, $\mathbf{D}$, $\mathbf{N}^{\mathbf{T}}$ and $\mathbf{M}^{\mathbf{T}}$ are the same as (7), $\mathbf{A}_s$ is the shear stiffness matrix

$$\mathbf{A}_s = \sum_{k=1}^{N}\left[\overline{Q}_s\right]^{(k)}\left(z_{k+1}-z_k\right) \tag{12}$$

in which

$$\left[\overline{Q}_s\right]^{(k)} = \begin{bmatrix}\overline{Q}_{44} & \overline{Q}_{45}\\ \overline{Q}_{45} & \overline{Q}_{55}\end{bmatrix}^{(k)} \tag{13}$$

The transverse shear forces are

$$\mathbf{T} = k_s\left[\mathbf{A_s}\right]\{\boldsymbol{\gamma}\} \tag{14}$$

where k_s is the shear correction factor.

III. FE Method

A. Interpolation Functions for Quadrilateral Elements

Four quadrilateral elements are introduced in this section. They are the 4-node conforming plate element for the CLPT, the 4-node and 9-node Mindlin plate element for the FSDT, and the displacement-based laminate element RDKQ-NL20 developed by Zhang el al. [19]. All the 4-node quadrilateral elements use linear Lagrange interpolation functions for the in-plane displacements but different interpolation functions for the bending deflections.

As shown in Fig. 2, the conforming rectangular element has six degrees of freedom per node. The linear Lagrange interpolation functions for the in-plane displacements are

$$\begin{Bmatrix} N_1 \\ N_2 \\ N_3 \\ N_4 \end{Bmatrix} = \frac{1}{4}\begin{Bmatrix} (1-\xi)(1-\eta) \\ (1+\xi)(1-\eta) \\ (1+\xi)(1+\eta) \\ (1-\xi)(1+\eta) \end{Bmatrix} \tag{15}$$

where (ξ,η) are the element coordinates, or called natural coordinates.

The Hermite cubic interpolations for the bending deflections are

$$\begin{aligned} g_{i1} &= \frac{1}{16}(\xi+\xi_i)^2(\xi\xi_i-2)(\eta+\eta_i)^2(\eta\eta_i-2) \\ g_{i2} &= \frac{1}{16}a\xi_i(\xi+\xi_i)^2(1-\xi\xi_i)(\eta+\eta_i)^2(\eta\eta_i-2) \\ g_{i3} &= \frac{1}{16}b\eta_i(\xi+\xi_i)^2(\xi\xi_i-2)(\eta+\eta_i)^2(1-\eta\eta_i) \\ g_{i4} &= \frac{1}{16}ab\xi_i\eta_i(\xi+\xi_i)^2(1-\xi\xi_i)(\eta+\eta_i)^2(1-\eta\eta_i) \end{aligned} \tag{16}$$

Here *a* and *b* are the sides of the rectangular element and (ξ_i,η_i) are the coordinates of the nodes in the (ξ,η) coordinate system. Thus, the displacements u_0, v_0, w_0 in the element can be approximated by nodal displacement as

$$u=\sum_{i=1}^{4}N_iu_i,\ v=\sum_{i=1}^{4}N_iv_i,\ w_0=\sum_{i=1}^{4}(g_{i1}w_i+g_{i2}\theta_{xi}+g_{i3}\theta_{yi}+g_{i4}\theta_{xyi}) \tag{17}$$

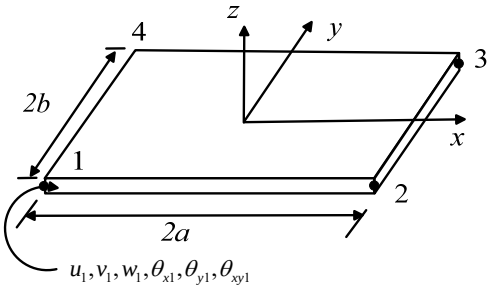

Fig. 2 A conforming rectangular element with six degrees of freedom $(u_i, v_i, w_i, \theta_{xi}, \theta_{yi}, \theta_{xyi})$ per node

The 4-node and the 9-node Mindlin plate elements have 5 degrees of freedom per node, as shown in Figs. 3 and 4, respectively. Therefore, the total degrees of freedom for 4-ndoe and 9-node FSDT element are 20 and 45, respectively. Because the weak forms of the first-order theory contain, at the most, only the first derivatives of the in-plane displacement and bending deflections; therefore, u_0, v_0, w_0, θ_x and θ_y can be approximated using the same Lagrange interpolation functions as

$$u=\sum_{i=1}^{n}N_iu_i, v=\sum_{i=1}^{n}N_iv_i, w_0=\sum_{i=1}^{n}N_iw_i, \theta_x=\sum_{i=1}^{n}N_i\theta_{xi}, \theta_y=\sum_{i=1}^{n}N_i\theta_{yi} \tag{18}$$

For the 4-node linear element, *n* equals 4 and N_i can be obtained from (15). For the 9-node quadratic element, *n* is 9 and N_i are expressed as

$$\begin{Bmatrix} N_1 \\ N_2 \\ N_3 \\ N_4 \\ N_5 \\ N_6 \\ N_7 \\ N_8 \\ N_9 \end{Bmatrix} = \frac{1}{4}\begin{Bmatrix} (1-\xi)(1-\eta)\xi\eta \\ -(1+\xi)(1-\eta)\xi\eta \\ (1+\xi)(1+\eta)\xi\eta \\ -(1-\xi)(1+\eta)\xi\eta \\ -2(1-\xi^2)(1-\eta)\eta \\ 2(1-\eta^2)(1+\xi)\xi \\ 2(1-\xi^2)(1+\eta)\eta \\ -2(1-\eta^2)(1-\xi)\xi \\ 4(1-\xi^2)(1-\eta^2) \end{Bmatrix} \tag{19}$$

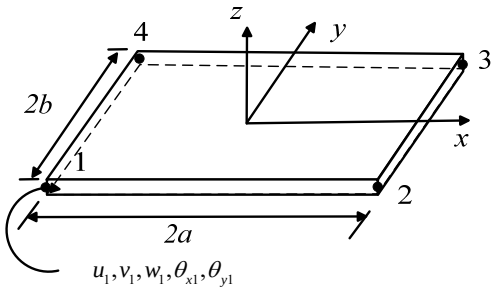

Fig. 3 A 4-node linear Lagrange rectangular elements with 5 degrees of freedom $(u_0, v_0, w_0, \theta_x, \theta_y)$ per node

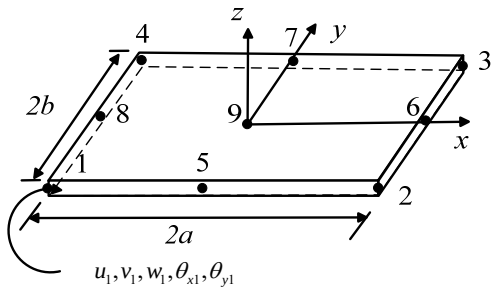

Fig. 4 A 9-node quadratic Lagrange rectangular elements with 5 degrees of freedom $(u_0, v_0, w_0, \theta_x, \theta_y)$ per node

It should be mentioned here that the conforming CLPT element does not consider the shear strain, which is not suitable for analysis of thick plate. The FSDT element assumes constant transverse shear strain/stress through the plate thickness, and requires shear correction factors to approximate actual stress states. As the thickness-span ratio of a laminate becomes small, shear locking may occur for 4-node Mindlin plate element. Although reduced integration and selectively reduced integration methods are proposed to eliminate this, it is found that the element often cannot pass the patch test for thin plates. To solve this, Zhang et al. [19] used the Timoshenko's beam function method to develop a 4-node 20 degrees of freedom quadrilateral laminated plate element without shear-locking, which is named as RDKQ-NL20.

The linear interpolation function (15) is adopted to describe the in-plane and out-of-plane displacements u_0, v_0, w_0 for the element RDKQ-NL20. The rotational displacements θ_x and θ_y are first carried as the nodal variables θ_{xi} and θ_{yi} by shape functions of the 8-node quadratic serendipity element. By using the Timoshenko's laminated composite beam functions, the rotational displacement parameters at mid-nodes are expressed by those of corner nodes. Thus, θ_x and θ_y are eventually written as

$$\begin{Bmatrix}\theta_x\\ \theta_y\end{Bmatrix}=\begin{bmatrix}\bar{N}_1 & \bar{N}_2 & \bar{N}_3 & \bar{N}_4\end{bmatrix}\{w_b\} \tag{20}$$

where

$$\{w_b\}^T=\{w_1 \quad \theta_{x1} \quad \theta_{y1} \quad w_2 \quad \theta_{x2} \quad \theta_{y2} \quad w_3 \quad \theta_{x3} \quad \theta_{y3} \quad w_4 \quad \theta_{x4} \quad \theta_{y4}\} \tag{21}$$

and

$$\bar{N}_i=\begin{bmatrix}P_i & P_{xi} & P_{yi}\\ Q_i & Q_{xi} & Q_{yi}\end{bmatrix} \quad (i=1,2,3,4) \tag{22}$$

The transverse shear strains can be expressed in terms of natural co-ordinates as

$$\{\gamma\}=[B_s]\{w_b\} \tag{23}$$

where $[B_s]$ is the shear strain matrix.

Detailed derivation of $P_i, P_{xi}, P_{yi}, Q_i, Q_{xi}, Q_{yi}$ and $[B_s]$ can be found in [19].

B. FE Formulation for Geometrically Nonlinear Analysis of Bistable Plates

The nonlinear FE equations for element RDKQ-NL20 are derived in this section and the FE model for other elements can be developed following the same way. For a plate subjected to thermal load, the total potential work based on the FSDT is

$$\delta W=\int_A \delta\begin{Bmatrix}\boldsymbol{\varepsilon}^0\\ \mathbf{k}\\ \boldsymbol{\gamma}\end{Bmatrix}^T\left(\begin{bmatrix}\mathbf{A} & \mathbf{B} & \mathbf{0}\\ \mathbf{B} & \mathbf{D} & \mathbf{0}\\ \mathbf{0} & \mathbf{0} & \mathbf{A_s}\end{bmatrix}\begin{Bmatrix}\boldsymbol{\varepsilon}^0\\ \mathbf{k}\\ \boldsymbol{\gamma}\end{Bmatrix}-\begin{Bmatrix}\mathbf{N^T}\\ \mathbf{M^T}\\ \mathbf{0}\end{Bmatrix}\right)dA=0 \tag{24}$$

where ρ, h, and A are the mass density, thickness and area of the plate element.

Using the interpolation functions (15), the membrane strain of the element is

$$\boldsymbol{\varepsilon}_{\mathbf{m}}^{\mathbf{0}}=\begin{Bmatrix}\frac{\partial u_0}{\partial x}\\ \frac{\partial v_0}{\partial y}\\ \frac{\partial u_0}{\partial y}+\frac{\partial v_0}{\partial x}\end{Bmatrix}=\begin{Bmatrix}\frac{\partial}{\partial x}[N_i]\\ \frac{\partial}{\partial y}[N_i]\\ \frac{\partial}{\partial y}[N_i]+\frac{\partial}{\partial x}[N_i]\end{Bmatrix}\{w_m\}=[B_m]\{w_m\} \tag{25}$$

in which

$$\{w_m\}=\{u_1 \quad v_1 \quad u_2 \quad v_2 \quad u_3 \quad v_3 \quad u_4 \quad v_4\}^T \tag{26}$$

and

$$[B_m]=\{B_{m1} \quad B_{m2} \quad B_{m3} \quad B_{m4}\}, B_{mi}=\begin{bmatrix}\frac{\partial N_i}{\partial x} & 0\\ 0 & \frac{\partial N_i}{\partial y}\\ \frac{\partial N_i}{\partial y} & \frac{\partial N_i}{\partial x}\end{bmatrix} \tag{27}$$

The nonlinear strain can be expressed as

$$\boldsymbol{\varepsilon}_{\mathbf{b}}^{\mathbf{0}}=\frac{1}{2}\begin{bmatrix}\frac{\partial w}{\partial x} & 0\\ 0 & \frac{\partial w}{\partial y}\\ \frac{\partial w}{\partial y} & \frac{\partial w}{\partial x}\end{bmatrix}\begin{Bmatrix}\frac{\partial w}{\partial x}\\ \frac{\partial w}{\partial y}\end{Bmatrix}=\frac{1}{2}[\theta]\{G\}=\frac{1}{2}[\theta][B_\theta]\{w_b\} \tag{28}$$

where

$$[B_\theta]=\{B_{\theta 1} \quad B_{\theta 2} \quad B_{\theta 3} \quad B_{\theta 4}\}, B_{\theta i}=\begin{bmatrix}\frac{\partial N_i}{\partial x} & 0 & 0\\ \frac{\partial N_i}{\partial y} & 0 & 0\end{bmatrix} \tag{29}$$

Using the interpolation functions (20), the bending strain can be rewritten as

$$\boldsymbol{\kappa}=\begin{Bmatrix}\dfrac{\partial\theta_x}{\partial x}\\ \dfrac{\partial\theta_y}{\partial y}\\ \dfrac{\partial\theta_x}{\partial y}+\dfrac{\partial\theta_y}{\partial x}\end{Bmatrix}=\left[B_b\right]\left\{w_b\right\} \tag{30}$$

where $\left[B_b\right]=\left\{B_{b1}\quad B_{b2}\quad B_{b3}\quad B_{b4}\right\}$ and

$$B_{bi}=\begin{bmatrix}\dfrac{\partial P_i}{\partial x} & \dfrac{\partial P_{xi}}{\partial x} & \dfrac{\partial P_{yi}}{\partial x}\\ \dfrac{\partial Q_i}{\partial y} & \dfrac{\partial Q_{xi}}{\partial y} & \dfrac{\partial Q_{yi}}{\partial y}\\ \dfrac{\partial P_i}{\partial y}+\dfrac{\partial Q_i}{\partial x} & \dfrac{\partial P_{xi}}{\partial y}+\dfrac{\partial Q_{xi}}{\partial x} & \dfrac{\partial P_{yi}}{\partial y}+\dfrac{\partial Q_{yi}}{\partial x}\end{bmatrix} \tag{31}$$

Combining the strain matrices (23), (27), (29) and (31) into one, the strain matrix of the element RDKQ-NL20 corresponding to the nodal displacement vector $\mathbf{u}=\left\{w_1\quad w_2\quad w_3\quad w_4\right\}$, $w_i=\left\{w_{mi}\quad w_{bi}\right\}$ is obtained as

$$B^e=B_0+B_l/2 \tag{32}$$

where B_0 is the linear strain matrix

$$B_0=\left[B_{01}\quad B_{02}\quad B_{03}\quad B_{04}\right],\ B_{0i}=\begin{bmatrix}B_{mi} & 0\\ 0 & B_{bi}\\ 0 & B_{si}\end{bmatrix} \tag{33}$$

The nonlinear strain matrix B_l is expressed as

$$B_{0i}=\begin{bmatrix}0 & B_{li}^b\\ 0 & 0\\ 0 & 0\end{bmatrix},\ B_{li}^b=\left[\theta\right]\left[B_{\theta i}\right] \tag{34}$$

The first variation of the strains in (24) is

$$\delta\begin{Bmatrix}\boldsymbol{\varepsilon}^0\\ \mathbf{k}\\ \boldsymbol{\gamma}\end{Bmatrix}^T=\tilde{B}^e\delta\mathbf{u}=\left(B_0+B_l\right)\delta\mathbf{u} \tag{35}$$

Substituting (32) and (35) into (24), and based on the TL approach, the nonlinear FE equations can be obtained as

$$\left(\mathbf{K}+\mathbf{K}_{\boldsymbol{\sigma}}\right)\Delta\mathbf{u}=-{}^{t}\mathbf{R} \tag{36}$$

where

$$\mathbf{K}=\sum_e\mathbf{K}^{\mathbf{e}},\ \mathbf{K}_{\boldsymbol{\sigma}}=\sum_e\mathbf{K}_{\boldsymbol{\sigma}}^{\mathbf{e}},\ {}^{t}\mathbf{R}=\sum_e{}^{t}\mathbf{R}^{\mathbf{e}} \tag{37}$$

$\mathbf{K}_{\sigma}^{\mathbf{e}}$ is the geometric stiffness matrix due to the geometric nonlinear deformation which can be calculated as

$$\mathbf{K}_{\boldsymbol{\sigma}}^{\mathbf{e}}=\begin{bmatrix}0 & 0\\ 0 & K_{\sigma ij}^b\end{bmatrix} \tag{38}$$

$$K_{\sigma ij}^b=\int_A B_{\theta i}^T\left[\sigma_l\right]B_{\theta j}dA \tag{39}$$

$$\left[\sigma_l\right]=\begin{bmatrix}N_x & N_{xy}\\ N_{xy} & N_y\end{bmatrix} \tag{40}$$

where $\mathbf{N}=\left[N_x\quad N_y\quad N_{xy}\right]^T=\mathbf{A}\boldsymbol{\varepsilon}^0+\mathbf{B}\boldsymbol{\kappa}-\mathbf{N}^{\mathbf{T}}$ is the in-plane forces.

The element internal force vector is calculated as

$${}^{t}\mathbf{R}^{\mathbf{e}}=\int_A\left[\tilde{B}^e\right]^T\left\{\sigma_e^*\right\}dA \tag{41}$$

in which $\left\{\sigma_e^*\right\}$ is the stress resultant after the i^{th} iteration and is calculated as

$$\left\{\sigma_e^*\right\}=\begin{bmatrix}\mathbf{A} & \mathbf{B} & \mathbf{0}\\ \mathbf{B} & \mathbf{D} & \mathbf{0}\\ \mathbf{0} & \mathbf{0} & \mathbf{A_s}\end{bmatrix}\left[B^e\right]{}^{t}\mathbf{u}-\begin{Bmatrix}\mathbf{N^T}\\ \mathbf{M^T}\\ \mathbf{0}\end{Bmatrix} \tag{42}$$

IV. Results and Discussion

Case I: The first case considers nonlinear bending of orthotropic plate subjected to uniformly load of intensity q_0. The geometric and material parameters used are listed in Table I. Two types of simply supported boundary conditions SS-1 and SS-3 are considered, which is illustrated in Fig. 5. For the 4-node Mindlin plate element, to eliminate shear-locking, reduced integration is used to evaluate the transverse shear stiffnesses. For the RDKQ-NL20 element, full integration is used for all stiffness matrices due to it is free of shear-locking. The shear correction coefficient for the RDKQ-NL20 and the 4-node Mindlin plate element is taken to be $k_s=5/6$. 50 load steps are used with the load incremental of 0.05, and a tolerance of 10^{-6} is used for convergence.

Convergence analysis is first carried out for four plate elements using different mesh sizes. The deflection at the center of the plate with $q_0=2.5$ is calculated and plotted in Fig. 6. It can be observed that the center deflection gradually convergence to a constant value with the increment of mesh size, and the 4-node and 9-node FSDT and RDKQ-NL20 element needs fewer elements to obtain a converge value than the CLPT element. Comparison of the load-displacement curve using a 10×10 mesh size for four elements is displayed in Fig. 7. It is obviously seen that four elements predict nearly the same results. Thus, the convergence and the accuracy of present FE model are checked.

TABLE I
GEOMETRIC AND MATERIAL PROPERTIES OF ORTHOTROPIC PANEL FOR CASE I.

Geometric properties	Material properties
Dimensions: $a = b = 12$in., $h = 0.138$in. Boundary conditions: SS-1 or SS-3	$E_1 = 3\times10^6$ psi $E_2 = 1.26\times10^6$ psi $G_{12} = G_{23} = G_{13} = 0.37\times10^6$ psi Poisson's ratio $\nu_{12} = 0.32$

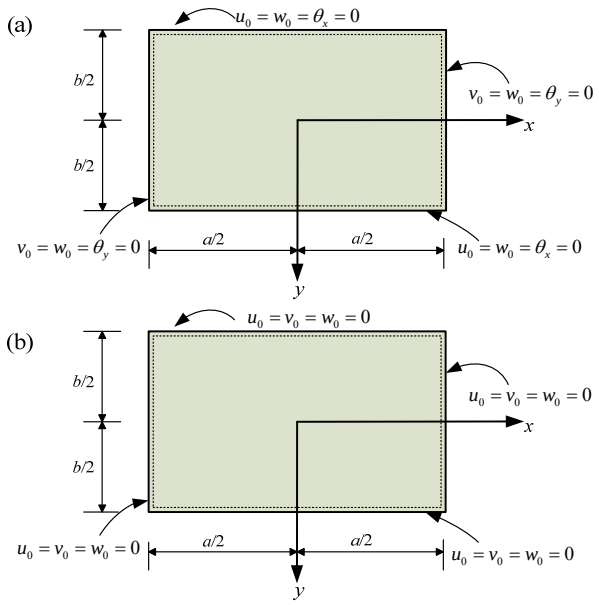

Fig. 5 Geometric boundary conditions used for (a) SS-1 type and (b) SS-3 type simply supported rectangular plates

Case II: The second case predicts cured shape of unsymmetric laminates subjected to thermal load. The composite laminates are made of T300/5208 graphite-epoxy with a stacking sequence of $[90/0]_T$, as shown in Fig. 8. The material properties for T300/5208 graphite-epoxy are listed in Table II [20]. The laminate is cooled from a curing temperature of 180°C to the room temperature of 25°C. Cured shape of a square laminate with length of 150mm is predicted by using the developed FE method and the commercial software package ABAQUS. The plate is modelled using 400 4-node quadrilateral shell element (S4R) with a total of 441 nodes. Boundary condition in the FE model is fixing the center node of the plate. It should be mentioned here that, in the FE model, the initial cured shape of the cross-ply laminates is always a saddle shape due to their symmetrical geometry. In order to make the square plate convergence to one of the stable shapes, some tricks should be taken [20], [21]. For examples, one can carry out buckling analysis and use the buckling mode as the initial nodal displacement, or apply small forces at the corner of the plate and then remove them after convergence results are obtained, or apply thermal load to the layer of the laminate one by one.

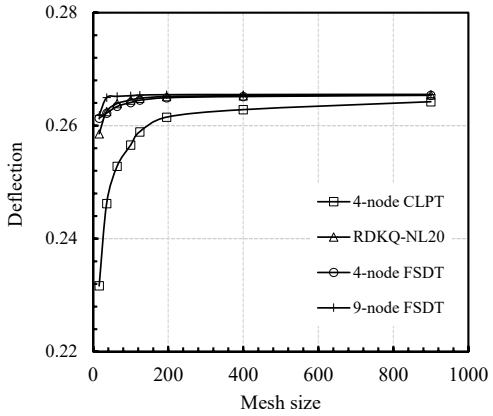

Fig. 6 Convergence analysis of deflection at the center of the plate with load of 2.5 for different mesh sizes

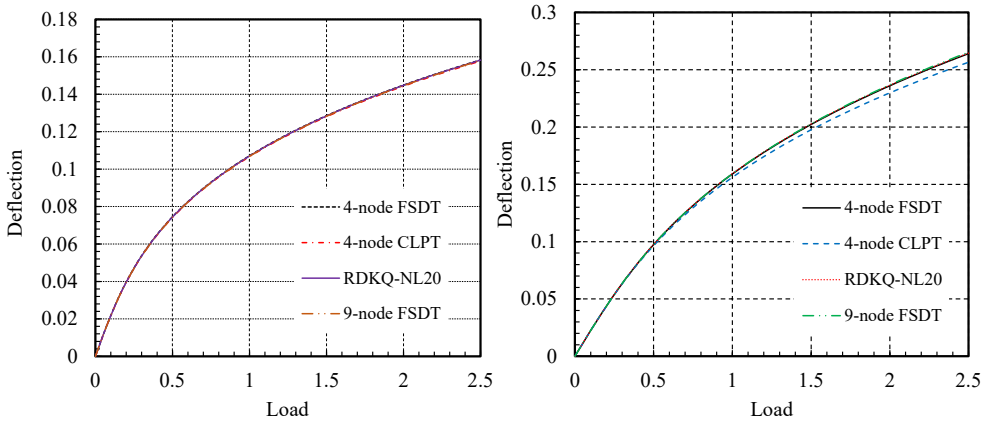

Fig. 7 Center deflection as functions of the load for simply supported, orthotropic, square plates under uniformly distributed load (10×10 mesh): (a) SS-3, (b) SS-1

The simulated stable shapes by four plate elements in our FE model (20×20 mesh) and the commercial software ABAQUS are listed in Table III. The curvatures can be approximated as

$$\kappa = \frac{8w}{l^2 + 4w^2} \tag{43}$$

where w is the out-of-plane deflection and l is the laminate chord length as shown in Fig. 9.

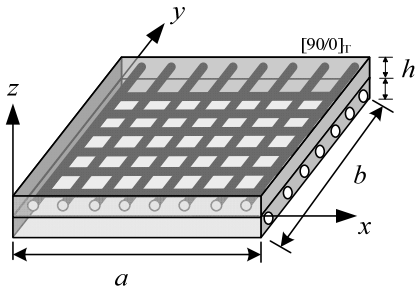

Fig. 8 Composite laminates with cross-ply stacking sequence.

It can be found from Table III that the 4-node CLPT plate element predicts a saddle shape while other plate elements based on FSDT predict two stable cylindrical shapes. The 4-node and 9-node Mindlin plate element and the RDKQ-NL20 plate element predict close curvatures compared to the results of ABAQUS. However, it should be mentioned here that, numerical experiments show that the convergence of the 4-node and 9-node Mindlin element is sensitive to the incremental steps and initial load. Among all the elements, the RDKQ-NL20 element shows the best accuracy and convergence in predicting stable shapes of bistable plate.

TABLE II
MATERIAL PROPERTIES OF T300/5208 GRAPHITE-EPOXY [20]

Material	Graphite-epoxy
E_{11}(GPa)	181
E_{22}(GPa)	10.3
G_{12}(GPa)	7.2
ν_{12}	0.28
$\alpha_1(10^{-6}/°C)$	-0.106
$\alpha_1(10^{-6}/°C)$	25.6
h(mm)	0.2

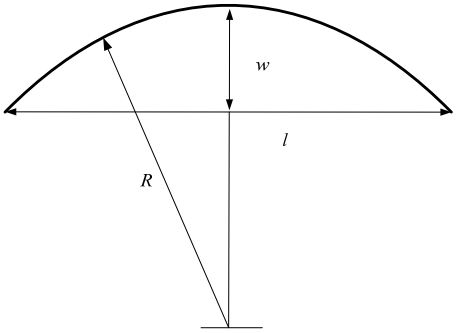

Fig. 9 Measurement of curvature in the FE model

TABLE III
SIMULATED STABLE SHAPES AND CURVATURES OF THE CROSS-PLY COMPOSITE LAMINATES

		Stable shapes	Curvature
Element types	4-node CLPT	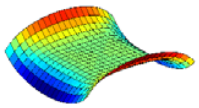	$\kappa_x = \kappa_y = -0.5944$
	4-node FSDT		$\kappa_x = -\kappa_y = -7.279$
	9-node FSDT		$\kappa_x = -\kappa_y = -6.917$
	RDKQ-NL20		$\kappa_x = -\kappa_y = 7.30$
	ABAQUS-S4R		$\kappa_x = -\kappa_y = 7.309$

V. CONCLUSION

Four quadrilateral plate elements based on the CLPT and the FSDT are used to formulate the nonlinear FE equations in order to predict the stable shapes of thermally-induced bistable plate. The convergence and accuracy of the developed FE model based on four plate elements are checked through calculating the nonlinear bending of orthotropic plate subjected to uniform load. Stable shapes of a square composite laminate with cross-ply stacking sequence under thermal load are simulated. All plate elements predict two cylindrical shapes except the 4-node

conforming plate element. The RDKQ-NL20 plate element shows the best accuracy and convergence compared to ABAQUS when equal mesh size is used. Therefore, the RDKQ-NL20 element shows great advantages in static analysis of thermally-induced bistable plate. The developed FE model using RDKQ-NL20 element can also be used to simulate static behaviors of other prestress-induced bistable plate, such as the voltage-induced piezoelectric bistable plate.

ACKNOWLEDGMENT

The financial supports from the Science and Technology Innovation Commission of Shenzhen Municipality (Ref: JCYJ20160229165310679) and the City University of Hong Kong (grant no 9680086), are gratefully acknowledged.

REFERENCES

[1] O. Bilgen, A. F. Arrieta, M. I. Friswell, and P. Hagedorn 2013 Dynamic control of a bistable wing under aerodynamic loading Smart. Mater. Struct. 22 025020
[2] X. Lachenal, S. Daynes, and P. M. Weaver 2013 Review of morphing concepts and materials for wind turbine blade applications Wind Energy. 16 283-307
[3] S. Daynes and P. M. Weaver 2013 Review of shape-morphing automobile structures: concepts and outlook P. I. Mech. Eng. D-J. Aut. 227 1603-1622
[4] A. F. Arrieta, P. Hagedorn, A. Erturk, and D. J. Inman 2010 A piezoelectric bistable plate for nonlinear broadband energy harvesting Appl. Phys. Lett. 97 104102
[5] A. F. Arrieta, T. Delpero, A. E. Bergamini, and P. Ermanni 2013 Broadband vibration energy harvesting based on cantilevered piezoelectric bi-stable composites Appl. Phys. Lett. 102 173904
[6] M. W. Hyer 1981 Some observations on the cured shape of thin unsymmetric laminates J. Compos.Mater. 15 175-194
[7] M.-L. Dano and M. W. Hyer 1998 Thermally-induced deformation behavior of unsymmetric laminates Int. J. Solids. Struct. 35 2101-2120
[8] W. Hufenbach, M. Gude, L. Kroll, A. Sokolowski, and B. Werdermann 2001 Adjustment of residual stresses in unsymmetric fiber-reinforced composites using genetic algorithms Mech. Compos. Mater. 37 71-78
[9] W. Hufenbach, M. Gude, and L. Kroll 2002 Design of multistable composites for application in adaptive structures Compos. Sci. Technol. 62 2201-2207
[10] M. Gigliotti, M. R. Wisnom, and K. D. Potter 2004 Loss of bifurcation and multiple shapes of thin [0/90] unsymmetric composite plates subject to thermal stress Compos. Sci. Technol. 64 109-128
[11] M.-L. Dano and M. W. Hyer 2002 Snap-through of unsymmetric fiber-reinforced composite laminates Int. J. Solids. Struct. 39 175-198
[12] C. G. Diaconu, P. M. Weaver, and A. F. Arrieta 2009 Dynamic analysis of bi-stable composite plates J. Sound. Vib. 322 987-1004
[13] Z. Zhang, H. Wu, G. Ye, J. Yang, S. Kitipornchai, and G. Chai 2016 Experimental study on bistable behaviour of anti-symmetric laminated cylindrical shells in thermal environments Compos. Struct. 144 24-32
[14] S. Daynes, K. Potter, and P. Weaver 2008 Bistable prestressed buckled laminates Compos. Sci. Technol. 68 3431-3437
[15] H. Li, F. Dai, P. M. Weaver, and S. Du 2014 Bistable hybrid symmetric laminates Compos. Struct. 116 782-792
[16] X. Q. He, L. Li, S. Kitipornchai, C. M. Wang, and H. P. Zhu 2012 Bi-Stable Analyses of Laminated Fgm Shells Int. J. Struct. Stab. Dy. 12 311-335
[17] Z. Zhang, B. Chen, C. Lu, H. Wu, H. Wu, S. Jiang, et al. 2017 A novel thermo-mechanical anti-icing/de-icing system using bi-stable laminate composite structures with superhydrophobic surface Compos. Struct. 180 933-943
[18] D. N. Betts, R. A. Guyer, P.-Y. Le Bas, C. R. Bowen, D. Inman, and H. A. Kim 2014 Modelling the Dynamic Response of Bistable Composite Plates for Piezoelectric Energy Harvesting
[19] Y. X. Zhang and K. S. Kim 2004 Two simple and efficient displacement-based quadrilateral elements for the analysis of composite laminated plates International Journal for Numerical Methods in Engineering. 61 1771-1796
[20] S. Tawfik, X. Tan, S. Ozbay, and E. Armanios 2006 Anticlastic Stability Modeling for Cross-ply Composites J. Compos.Mater. 41 1325-1338
[21] A. Haldar, J. Reinoso, E. Jansen, and R. Rolfes 2018 Thermally induced multistable configurations of variable stiffness composite plates: Semi-analytical and finite element investigation Compos. Struct. 183 161-175 G. O. Young, "Synthetic structure of industrial plastics (Book style with paper title and editor)," in *Plastics*, 2nd ed. vol. 3, J. Peters, Ed. New York: McGraw-Hill, 1964, pp. 15–64.